Journal of Manufacturing Processes 26 (2017) 240–251

Contents lists available at ScienceDirect

Journal of Manufacturing Processes

journal homepage: www.elsevier.com/locate/manpro

Technical Paper

Three-dimensional mapping of the residual stress field in a locally-rolled aluminium alloy specimen

H.E. Coules [a,*], G.C.M. Horne [a], S. Kabra [b], P. Colegrove [c], D.J. Smith [a,1]

[a] Department of Mechanical Engineering, University of Bristol, Bristol, BS8 1TR, UK
[b] ISIS Facility, STFC Rutherford Appleton Laboratory, Didcot, Oxfordshire, OX11 0QX, UK
[c] School of Applied Sciences, Cranfield University, Cranfield, Bedfordshire, MK43 0AL, UK

ARTICLE INFO

Article history:
Received 15 December 2016
Received in revised form 14 February 2017
Accepted 16 February 2017
Available online 8 March 2017

Keywords:
Residual stress
Neutron diffraction
Finite element analysis
Rolling
Welding

ABSTRACT

Detrimental residual stresses that occur in welded joints can be removed by rolling the weld seam. In this study we show that rolling could be applied to much thicker-section welds than has previously been attempted. A residual stress field introduced by localised rolling of an aluminium alloy specimen was studied to establish whether the plastic deformation caused by rolling would be sufficient to treat thick-section welds. It was modelled using finite element analysis and characterised using detailed neutron diffraction measurements. During rolling, plastic deformation occurs through the entire thickness of the specimen and strongly compressive residual stresses are created in the rolled area. Some features of the three-dimensional residual stress field, such as a region of tensile stress beyond the end of the rolled area, could be detrimental to structural integrity. It is recommended that these should be taken into account in the design of rolling-based weld treatment and surface treatment processes.

© 2017 The Authors. Published by Elsevier Ltd on behalf of The Society of Manufacturing Engineers. This is an open access article under the CC BY license (http://creativecommons.org/licenses/by/4.0/).

1. Introduction

Even in the absence of externally-applied loads, residual stresses can linger inside materials due to internal strain incompatibility. Residual stresses strongly affect a range of material behaviours and failure mechanisms including brittle fracture and fatigue fracture [1]. As a result, accurate residual stress characterisation is often crucial for the design and analysis of high-reliability mechanical components [2,3], and for the development of fabrication processes such as welding [4] and metal additive manufacturing [5]. In general, tensile residual stress normal to the plane of a crack-like defect increases the propensity for propagation of the crack. Therefore the presence of large tensile residual stresses in any part of a structure known to have an increased likelihood of defects, such as a weld seam, is undesirable.

Localised high-pressure rolling of metals can produce non-uniform plastic deformation in the rolled region. As a result, rolling can be used to modify the distribution of residual stress. This the basis for common surface treatments such as roller burnishing and deep rolling. Burnishing and deep rolling treatments involve deforming a region of material at the surface of a component using a small, hard, spherical or cylindrical tool of a few millimetres in diameter. This generates compressive residual stresses at the material's surface [6,7]. The compressive residual stress, and any associated surface hardening and smoothing, can impart improved fatigue resistance [8]. The depth over which the residual stresses resulting from these processes act is small: typically less than 1 mm [9–11].

Recently, it has been shown that localised rolling can be used to mitigate the tensile residual stresses which characteristically arise in welded joints during manufacture [12–16]. Large residual stresses may occur throughout the thickness of a joint, but small-scale burnishing-type treatments are not able to reach the material deep inside in thick-section welds. A process which causes much deeper and more extensive plasticity is required. Experimental studies by Altenkirch et al. [12] and Coules et al. [13,14] have shown that residual stress mitigation in weld seams can be achieved using a large, highly-loaded but freely-rotating roller to cause extensive plastic deformation of the weld region. This extensive plasticity causes weld-induced residual stresses to relax. The roller is applied directly to the weld seam, after welding. For welds in relatively thin structural steel and aluminium alloy (<10 mm thickness), this form of roller treatment can greatly reduce the residual stress present in the weld seam. With a sufficiently large rolling load the residual stress distribution may even be inverted, creating a zone of compressive residual stress along the weld [13]. This form of rolling is also being investigated for application to metal additive manu-

* Corresponding author.
E-mail address: harry.coules@bristol.ac.uk (H.E. Coules).
[1] Deceased.

http://dx.doi.org/10.1016/j.jmapro.2017.02.010
1526-6125/© 2017 The Authors. Published by Elsevier Ltd on behalf of The Society of Manufacturing Engineers. This is an open access article under the CC BY license (http://creativecommons.org/licenses/by/4.0/).

factured structures, and has been shown to improve the residual stress state [17,18], and microstructure [19,20], and to reduce the incidence of porosity defects [21].

Both the small-scale roller burnishing/deep rolling methods and the larger-scale weld rolling technique rely on the ability of the roller to produce plastic deformation in the workpiece. Although it is well-established that rolling contact can introduce compressive residual stresses at a material's surface [22], little work on the three-dimensional nature of the resulting stress field has been performed. Consequently, it is not clear whether detrimental patterns of residual stress may arise at the edges of the rolled/burnished areas. For deep rolling and roller burnishing, the lack of detailed experimental information can be attributed to the difficulty in measuring residual stress fields over the length scale involved (<1 mm from the surface). Most experimental measurements of residual stress introduced by deep rolling are made using Incremental Centre Hole Drilling (ICHD) or conventional X-ray diffraction, which are the most appropriate and accessible techniques for this length scale [23]. These techniques only provide a limited (typically one-dimensional) characterisation of the residual stress field. The larger-scale residual stress fields which occur after localised rolling of welds allow for more advanced residual stress measurement techniques to be used, including neutron diffraction and synchrotron X-ray diffraction [12,13]. However, the characterisation of rolled welds has so far focussed on sheet/strip metals less than 10 mm thick. There has also been a focus on the distribution of residual stress transverse to the rolling direction, rather than on the through-depth distribution of stress. As a result, it is unclear whether rolling can reduce the residual stresses present deep inside thick-section welds [24].

In this study, we examine the applicability of localised rolling for the stress relief of welds in thick-section materials. Specifically, we examine the depth to which plasticity and residual stress can be introduced using rolling, and the nature of the three-dimensional field of residual stress which arises. For welds, it is desirable to produce relaxation of weld-induced residual stresses throughout the thickness of the weld in order to prevent tensile residual stress from promoting the initiation of failure at internal weld defects. Using measurements from a specimen of homogenous, non-welded material subjected to localised rolling, we demonstrate that this process can produce plasticity deep inside the material.

2. Method

2.1. Overview

A rectangular aluminium alloy plate was rolled along its centreline using a large, narrow roller applied with a constant force and rolling velocity. Characterisation of the mechanical properties of the plate material was performed. The rolling process was simulated using the finite element method in order to predict the residual stress field in the rolled specimen. Neutron diffraction was used to measure the complete residual stress tensor at a large number of locations inside the rolled specimen and ICHD measurements were performed at the surface. Using the finite element model and measured results, the applicability of the rolling method for residual stress modification was assessed.

2.2. Rolled plate

The specimen was a $204 \times 153 \times 25$ mm oblong piece of aluminium alloy 6082-T6. It was cut from a larger plate with the grain oriented in the direction of the longest dimension. The machine used for rolling is described by Coules [24] and Coules et al. [13]. The specimen was rolled on one surface using a cylindrical roller

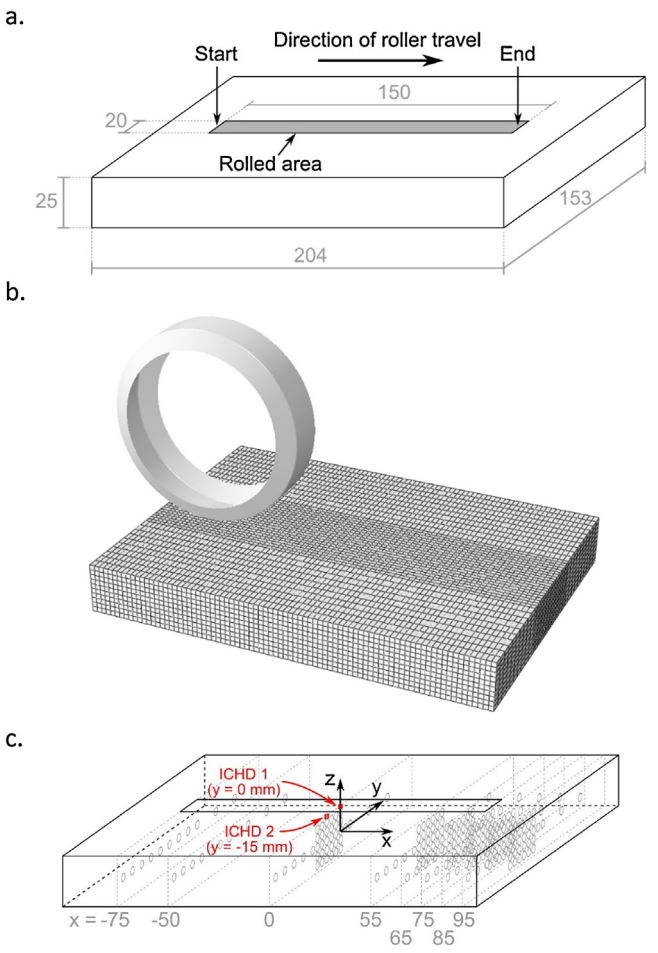


Fig. 1. a.) Geometry of the rolled aluminium alloy specimen showing the rolled region. b.) Finite element model of the rolling process. c.) Neutron diffraction measurement locations (grey circles) and ICHD measurement locations (red markers). Dimensions in mm.

of hardened AISI Type H13 tool steel with a diameter of 100 mm and an axial width of 20 mm. The roller was brought into contact with the upper surface of the specimen (Fig. 1b) and then a vertical force of 150 kN was applied to it. It was translated 150 mm along the specimen's length at a velocity of 8.3 mm s^{-1} while maintaining the constant 150 kN vertical force. Finally the roller was raised, having indented a rectangular region of the specimen's upper surface (Fig. 1a). Throughout this process, the roller was allowed to rotate freely on its axis. During rolling, the specimen was supported on its lower surface by the rigid steel bed of the rolling machine. An end stop bolted to the machine bed was used to prevent the specimen from moving in the rolling direction.

2.3. Material characterisation

Two types of mechanical test were performed to provide the material stress-strain characteristics required for the FE modelling: monotonic uniaxial tests and fully-reversed cyclic uniaxial tests. Both types of test were performed at ambient temperature.

For the monotonic tests, cylindrical specimens of un-deformed plate material were cut from the same batch of material as the rolled plate. The specimens had a parallel length of 28 mm, a diameter of 5 mm, and conformed to BS EN ISO 6892-1:2009 [25]. They were tested in tension to failure at a constant elongation rate of 3.33 μm s^{-1}. Testing was performed using an Instron 1340-series tensile testing machine and an iMetrum video extensometer system. Tensile specimens longitudinal and transverse to the grain of

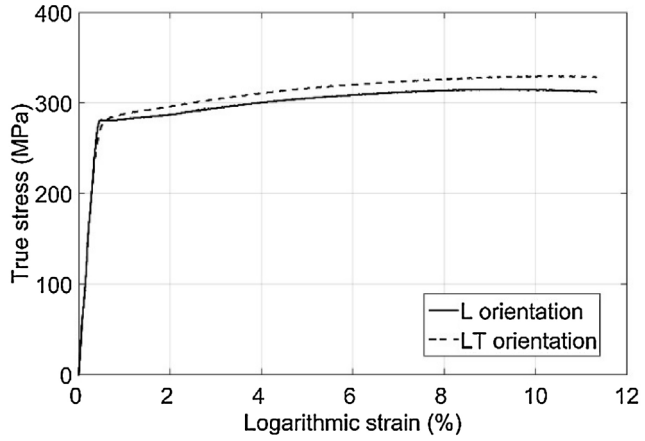


Fig. 2. Representative stress/strain curves determined from tensile tests of the specimen material with specimens oriented longitudinal and transverse to the grain direction.

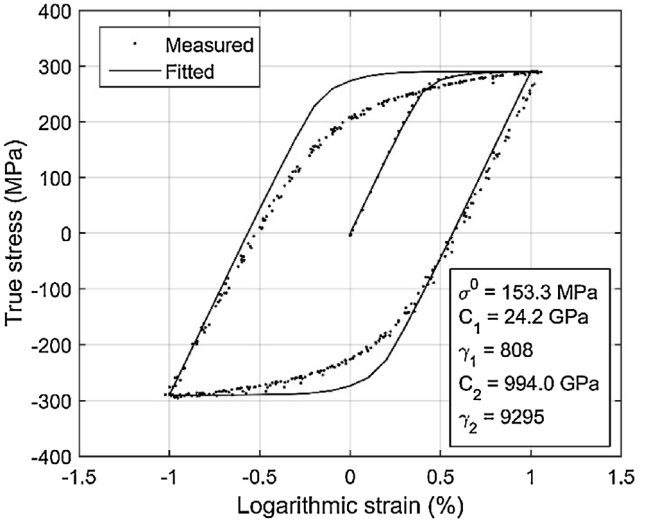


Fig. 3. Cyclic uniaxial stress-strain response of aluminium alloy 6082-T6 for a strain range of ±1%. The response of a fitted Chaboche non-linear kinematic hardening model is also shown.

the material were tested (L and LT orientations), with three specimens in each direction. Results for the monotonic tests are shown in Fig. 2. The stress-strain curves for the longitudinal and transverse directions are very similar and so the material was modelled as directionally isotropic in the finite element model described in Section 2.4. The elastic modulus was determined to be 67.1 GPa.

For the cyclic hardening tests, cylindrical uniaxial test specimens with a parallel length of 30 mm and a diameter of 7.5 mm were used. The specimens were deformed cyclically using a strain amplitude of ±1% in the gauge region at a strain rate of $\pm 5 \times 10^{-4}\ s^{-1}$, for 10 cycles. The cyclic tests were performed on the same Instron 1340-series load frame as the monotonic tests and the strain was measured using an Epsilon Technology clip extensometer. Three specimens were tested, all of which were in the LT orientation.

A representative result from the cyclic tests is shown in Fig. 3. The material shows almost no cyclic hardening in the strain range tested. In the finite element model of the rolling process described in Section 2.4, the material was modelled using a Chaboche non-linear kinematic hardening law [26,27]. In this material model, yielding is assumed to obey the von Mises criterion and the translation of the yield surface due to material hardening is described by the total backstress tensor α_{ij}. The yield surface is therefore described by the function:

The yield surface is therefore described by the function:

$$\sqrt{\frac{3}{2}\left(\sigma_{ij}^{dev}-\alpha_{ij}^{dev}\right)\left(\sigma_{ij}^{dev}-\alpha_{ij}^{dev}\right)}-\sigma^{0}=0 \quad (1)$$

where σ^0 is the material's initial yield stress. σ_{ij}^{dev} and α_{ij}^{dev} are the deviatoric components of the stress and backstress tensors respectively:

$$\sigma_{ij}^{dev}=\sigma_{ij}-\frac{1}{3}\sigma_{kk}\delta_{ij}$$

$$\alpha_{ij}^{dev}=\alpha_{ij}-\frac{1}{3}\alpha_{kk}\delta_{ij} \quad (2)$$

where σ_{ij} is the stress tensor and δ_{ij} is the Kronecker delta. The backstress tensor α_{ij} may be expressed as the sum of k individual backstress tensors: $\alpha_{ij}=\sum_{k}\alpha_{ijk}$. The total backstress is assumed to vary in response to plastic deformation according to:

$$\dot{\alpha}_{ij}=C_k\frac{1}{\sigma^0}(\sigma_{ij}-\alpha_{ijk})\dot{\bar{\varepsilon}}^{pl}-\gamma_k\alpha_{ijk}\dot{\bar{\varepsilon}}^{pl} \quad (3)$$

where $\dot{\alpha}_{ij}$ is the rate of the total backstress tensor, $\dot{\bar{\varepsilon}}^{pl}$ is the rate of the von Mises equivalent plastic strain, and C_k and γ_k are material-specific parameters. In this study the material was represented using a 2-backstress model (k = 1, 2), allowing the material's non-linear behaviour to be specified using five parameters: σ^0, C_1, γ_1, C_2 and γ_2.

A model of a single element of material undergoing cyclic uniaxial deformation in the same range as used in the cyclic hardening tests was created. This model was used to determine values for the parameters σ^0, C_1, γ_1, C_2 and γ_2 to closely represent the material, based on initial estimates from hardening parameter fitting utilities provided in Abaqus/Standard. The specimen material only undergoes a single stress reversal during the rolling process described in Section 2.2. Therefore, in fitting the parameters for the material model, priority was given to achieving the best possible fit to the first 2 quarter-cycles of the cyclic test data, while maintaining an acceptable correspondence with the data for later cycles.

2.4. Finite element model of the rolling process

The rolling process was simulated using finite element analysis in order to predict the residual stress field, and to examine the pattern of plasticity which occurs in the specimen during and after rolling. Although the residual stress field can be measured using neutron diffraction, there is no straightforward means to measure the 3D distribution of total plastic deformation in the specimen, and so modelling was used. The rolling process was modelled using the same sequence of operations as occurred in the real rolling process described in Section 2.2: lowering of the roller, translation under constant vertical force, and finally raising of the roller. During modelling, the specimen was assumed to be initially free of residual stress, and the Abaqus/Standard 6.12 solver [28] was used to perform the finite element calculations.

The specimen was represented in three dimensions using 98,400 8-noded reduced-integration linear brick elements, as shown in Fig. 1b. Sensitivity studies confirmed that the modelling result was insensitive to further mesh refinement beyond this level. The plate material was modelled with the time-independent Chaboche non-linear kinematic hardening model described in Section 2.3. The

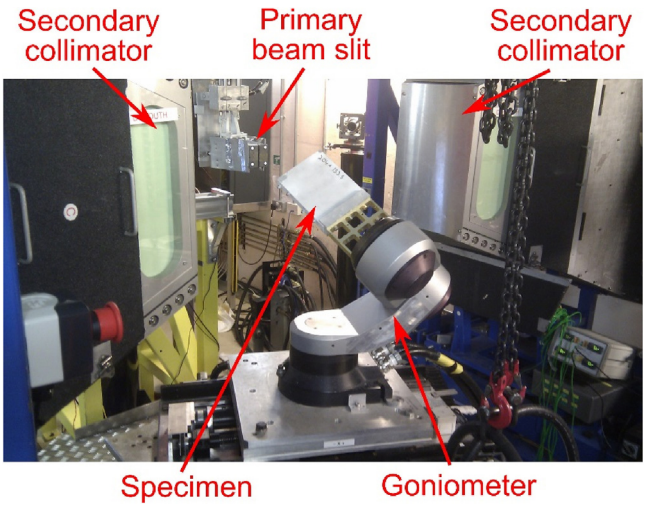


Fig. 4. Rolled plate specimen (painted white to allow specimen alignment using 3D laser scanning) set up and ready for measurement using the ENGIN-X neutron diffractometer. The goniometer was used to manipulate the specimen to achieve the scattering vectors shown in Fig. 5.

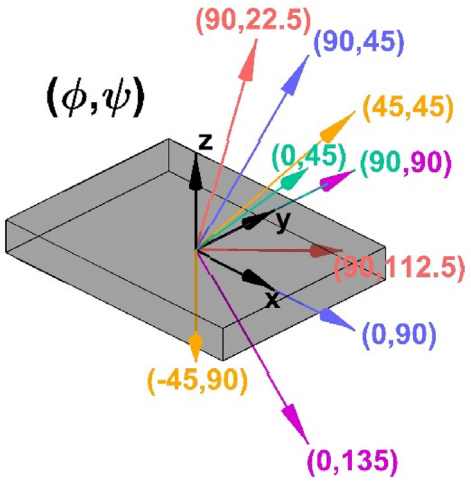


Fig. 5. Directions in which residual elastic strain was measured using neutron diffraction at the points shown in Fig. 1c. Angles in degrees. Pairs of arrows with the same colour indicate measurements made simultaneously using the two detector banks of ENGIN-X. Two sets of measurements were taken in the direction (90,90).

roller, machine bed and end stop were all modelled as rigid bodies in contact with the specimen plate. At all contact interfaces, Coulomb-model friction was assumed with a frictional coefficient of 0.5: an approximate value for unlubricated aluminium-steel contact [29,30]. Sensitivity studies showed that the resulting residual stress field was not sensitive to the frictional coefficient.

2.5. Residual stress measurements

During the measurement of residual stress by neutron diffraction [31–33], the material's mean lattice parameter, or the mean spacing of a particular lattice plane family, is determined from the distribution of scattered neutrons. The result is a spatial average of lattice parameter for favourably-oriented crystallites over a gauge volume within the specimen defined by the instrument optics, typically a few mm^3. To determine the continuum-scale elastic strain, this measurement is used together with a reference measurement from similar material in an unstressed state:

$$\varepsilon^{lmn} = \frac{a^{lmn} - a_0^{lmn}}{a_0^{lmn}} \tag{4}$$

where a^{lmn} and a_0^{lmn} are lattice parameters of the main specimen and the unstressed material respectively in a direction defined by the vector $[l, m, n]$, and ε^{lmn} is the elastic strain in the same direction.

Measurements of residual elastic strain in the rolled plate were performed using the ENGIN-X time-of-flight neutron diffractometer [34] at the ISIS pulsed neutron source (STFC Rutherford Appleton Laboratory, UK). The instrument setup is shown in Fig. 4. The measurement locations within the specimen are shown as grey circles in Fig. 1c. At each point, the elastic strain was measured in nine directions using a roughly cuboid gauge volume of $4 \times 4 \times 4$ mm. These directions are shown in Fig. 5. In one direction, a repeat measurement was performed so that there were a total of ten strain measurements at each point. Pawley-type structure refinement was performed using the GSAS refinement package [35] to determine the lattice parameter from each diffraction pattern. From these lattice parameters, the elastic strain in each measurement direction was found using Eq. (4). Strain transformation equations were used to relate the elastic strain in each measured direction (ε^{lmn}) to the six independent components of elastic strain tensor [31,32,36]:

$$\begin{aligned}\varepsilon^{lmn} = {} & \varepsilon_{xx}\sin^2\psi\cos^2\phi + \varepsilon_{yy}\sin^2\psi\sin^2\phi + \varepsilon_{zz}\cos^2\psi \\ & + 2\varepsilon_{xy}\sin^2\psi\sin\phi\cos\phi \\ & + 2\varepsilon_{yz}\sin\psi\cos\psi\sin\phi + 2\varepsilon_{zx}\sin\psi\cos\psi\cos\phi\end{aligned} \tag{5}$$

Where ε_{xx}, ε_{yy} etc. are the components of the elastic strain tensor, ϕ is the azimuth measured anticlockwise from the x axis, and ψ is the angle between the strain direction $[l, m, n]$ and the z axis. The complete strain tensor was then found by solving the resulting over-determined system of simultaneous linear equations for each measurement location in a least-squares sense [37,38]:

$$\varepsilon_j = A_{ij}^{+}\varepsilon_i^{lmn} \tag{6}$$

where ε_j is the elastic strain tensor written as a six-component vector, ε_i^{lmn} is a vector of the measured normal strains in the directions shown in Fig. 5, A_{ij} is a matrix of rotation cosines constructed using Eq. (5), and the superscript + denotes the Moore-Penrose pseudo-inverse. The error of each of the measured normal strains ε_i^{lmn} with respect to the strain tensor defined by ε_j was found using:

$$\Delta\varepsilon_i^{lmn} = \varepsilon_i^{lmn} - A_{ij}\varepsilon_j \tag{7}$$

where $\Delta\varepsilon_i^{lmn}$ is a vector of the differences between the ten measured strains and the strain tensor ε_j resolved in each measurement direction.

The stress tensor at each measurement point was determined from the strain tensor using Hooke's law for an isotropic material:

$$\sigma_{ij} = 3K\left(\frac{1}{3}\varepsilon_{kk}\delta_{ij}\right) + 2G\left(\varepsilon_{ij} - \frac{1}{3}\varepsilon_{kk}\delta_{ij}\right) \tag{8}$$

Where ε_{ij} is the elastic strain tensor (in 9-element tensor form as opposed to the vector form ε_j used in Eqs. (6) and (7)), K is the bulk modulus of the material, and G is the shear modulus. The bulk modulus is given by:

$$K = \frac{E}{3(1-2\nu)} \tag{9}$$

and the shear modulus by:

$$G = \frac{E}{2(1+\nu)} \tag{10}$$

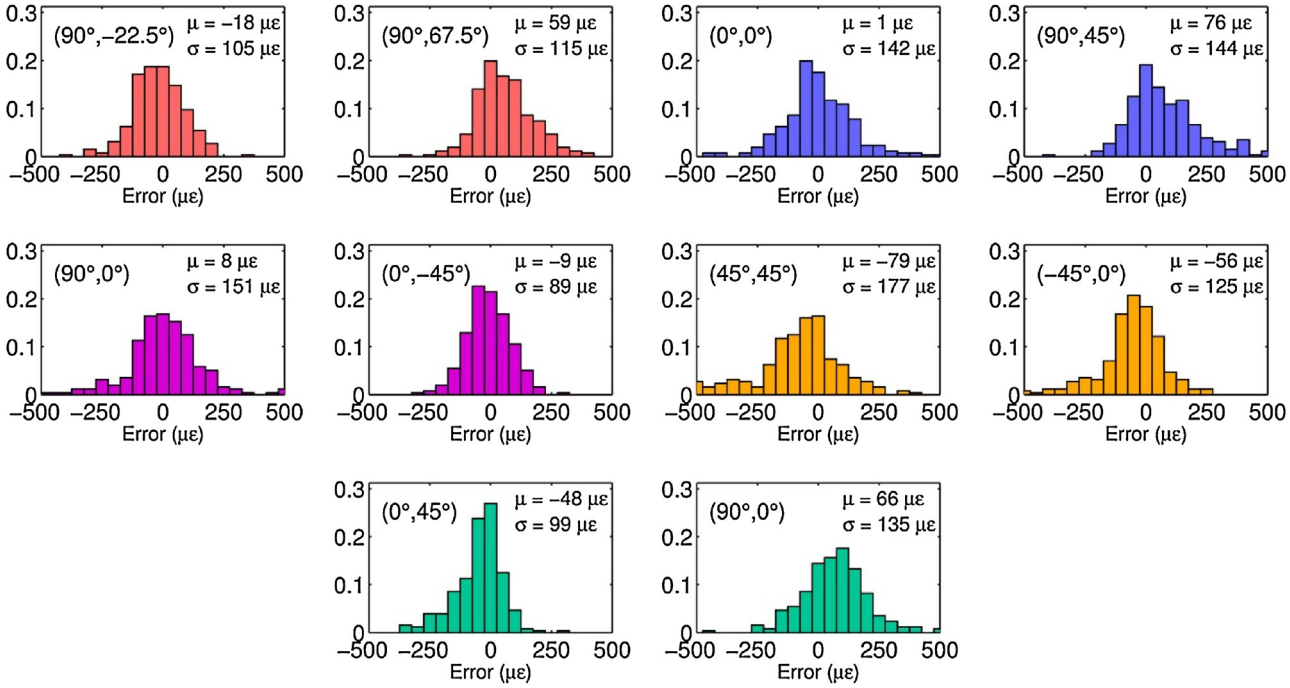


Fig. 6. Distributions of the error $\Delta\boldsymbol{\varepsilon}_i^{lmn}$ between measured strain at each measurement angle ($\boldsymbol{\varepsilon}_i^{lmn}$) and the corresponding strain tensor evaluated using the strains from all ten angles ($A_{ij}\varepsilon_j$), for the total population of 256 measurement points. The colour of each histogram corresponds to the colour of vectors shown in Fig. 5.

where E is the elastic modulus of the material and ν is the Poisson's ratio. It has been shown by Daymond et al. [39] that for lattice parameter changes characterised using time-of-flight neutron diffraction and Rietveld-type structure refinement, the continuum-scale elastic constants are well-representative of the relationship between the stress tensor and the apparent strain tensor.

The measurements of the unstrained lattice parameter a_0^{lmn} in Eq. (4) were taken from a comb-type sample cut using wire electrical discharge machining from a nominally-identical rolled specimen [40]. Separate a_0 measurements were performed for each measurement orientation. Positioning of both the main specimen and the a_0 comb to achieve the correct scattering vectors was carried out using an auxiliary goniometer stage. The virtual laboratory software SScanSS [41] was used to calculate the goniometer and positioning stage coordinates necessary to achieve the measurements.

Calculated uncertainties in lattice parameter determination were propagated through the calculation of the strain and stress tensors, as described in [42] and [43,44]. However, several other sources of uncertainty were not considered in these calculations. These factors include uncertainty in sample positioning, uncertainty in the elastic properties of the material and effects of grain size and material anisotropy. Also, each of the two banks of detectors on ENGIN-X covers a finite angular range. Therefore, each directional strain measurement represents the elastic strain averaged over a solid angle of approximately $\frac{\pi}{5}$ sr around each of the directions shown in Fig. 5 [34]. However, the measured strains were taken to be representative of these directions and the effect of angular strain averaging was assumed to be insignificant.

ICHD residual stress measurements according to ASTM E837-13a [45] were performed at two locations on the upper surface of the specimen (see Fig. 1c). These were used to determine the near-surface stress state, which is difficult to measure using neutron diffraction.

3. Results and discussion

3.1. Uncertainty analysis for the neutron diffraction measurements

After determining the elastic strain tensor at each measurement location shown in Fig. 1c from the measured directional strain data using Eq. (6), the misfit between this fitted strain tensor and the measured directional strains was evaluated using Eq. (7). The histograms in Fig. 6 show the frequency distribution of this misfit over the population of 256 measurement points, for each of the ten measurement directions. The mean error value and standard deviation of errors is also shown.

The predicted uncertainty in each directional strain measurement, calculated from the fitting uncertainty involved in determination of the lattice parameter (see Section 2.5), was between 30 and 45 $\mu\varepsilon$ for almost all of the measurements. However, the results in Fig. 6 show that the discrepancies between each measured directional strain and the fitted strain tensor resolved in the same direction is in general much larger than this. In fact, there may be a consistent offset of up to 79 $\mu\varepsilon$ in addition to normally-distributed errors with a standard deviation of 177 $\mu\varepsilon$. Therefore, the true uncertainty in individual components of the stress tensor calculated from the neutron diffraction measurements is likely to be in the region of 15–20 MPa, rather than the approximately 3 MPa implied by uncertainty in lattice parameter fitting alone. The error involved in determining lattice parameters from least-squares fitting of the neutron diffraction patterns forms only a small part of the overall uncertainty in strain tensor determination; other sources of uncertainty including those listed in Section 2.5 are much more significant.

3.2. Residual stress

The spatial density of the neutron diffraction measurements was highest on the planes x = 0, 50, 65, 75, 85 and 95 mm, where

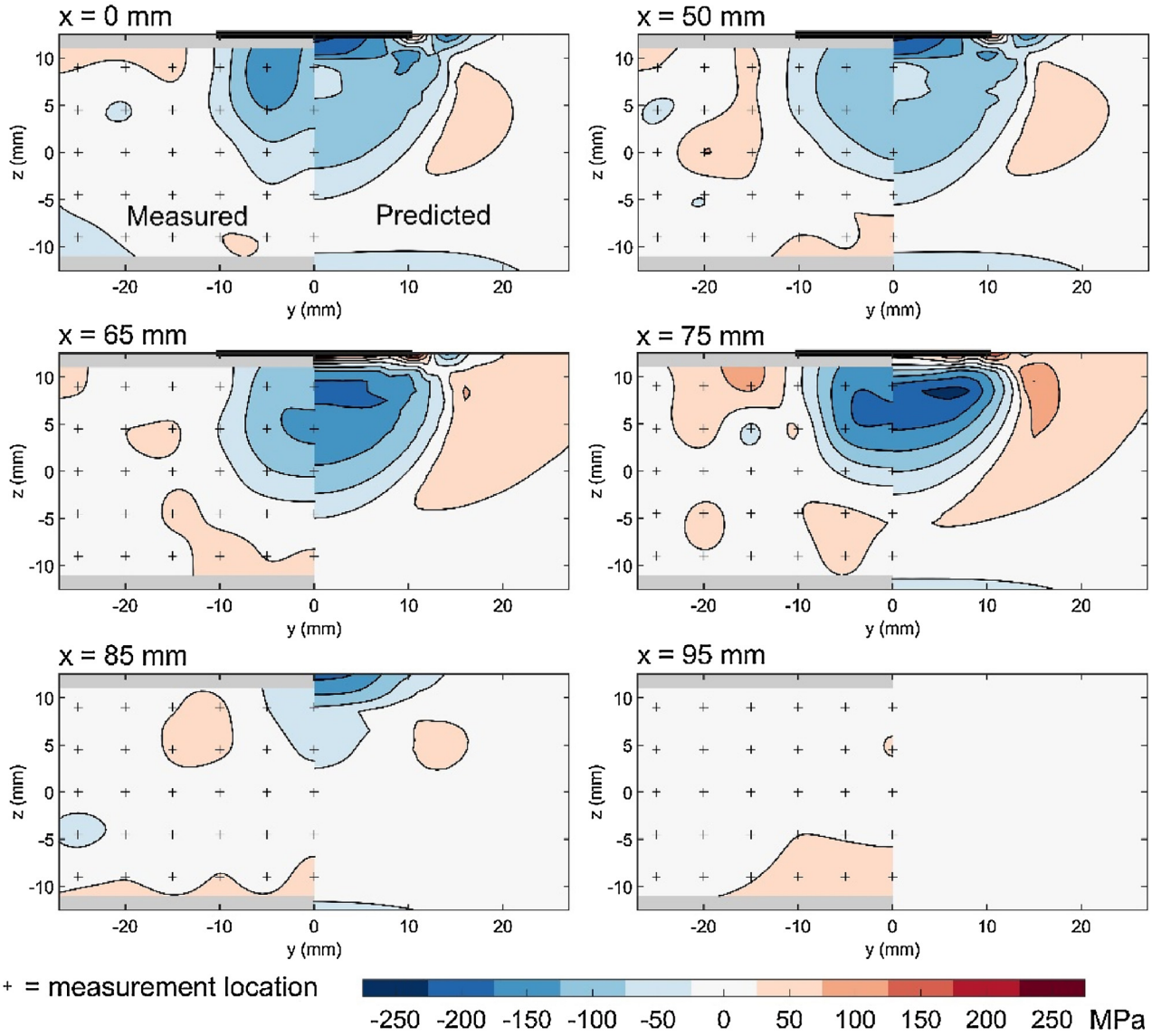


Fig. 7. Longitudinal residual stress (σ_{xx}) on six y-z planes within the specimen. Black crosses indicate neutron diffraction gauge volume centres and black lines at z = 12.5 indicate the roller contact zone.

x = 0 mm is at the mid-length of the specimen as shown in Fig. 1c. On these planes, two-dimensional arrays of measurement locations were used to map the residual stress field in a region close to the roller path on one side of the specimen. Figs. 7–9 show contour plots of the σ_{xx}, σ_{yy} and τ_{yz} components of the stress tensor respectively. The other components of the stress tensor (σ_{zz}, τ_{xy} and τ_{xz}) were found to have a relatively low magnitude throughout the measured area, and so are not shown. Results from both the FE model described in Section 2.4, and the neutron diffraction measurements described in Section 2.5, are presented. The measured results have been interpolated and the locations of the gauge volume centres used for measurement are shown as crosses.

The agreement between the predicted and measured residual stress fields shown in Figs. 7–9 is relatively good. The model and measurements agree well on the position of the main features of the residual stress field and their magnitudes. The neutron diffraction measurements were performed using a relatively low spatial resolution: only 5 and 4.5 mm in the y and z directions respectively, with a gauge volume of $4 \times 4 \times 4$ mm. Consequently, the measured data do not show as much detail in the residual stress field as is visible in the modelling result. Furthermore, the neutron diffraction data show some scatter, as discussed in Section 3.1, the result of which can be more easily seen in the line plots of Fig. 10. However, taking into account the limitations of the measurement technique, and given that *a priori* estimates of residual stress fields generated using elastic-plastic FEA are known to be strongly sensitive to parameters including the material constitutive model [15,46,47], the agreement between the measured and modelled data is good.

The main feature of the residual stress field is a region of strongly compressive stress under the roller's path. It is caused by plastic flow of material beneath the roller in the in-plane directions as it is compressed in the out-of-plane (z) direction. This feature is clearly visible in the plots of σ_{xx} (Fig. 7) and σ_{yy} (Fig. 8). The subfigures showing stress at x = 0 mm (i.e. half-way along the rolled region) give some idea of the residual stress field introduced by rolling in the steady-state, away from the start and end of the rolled area. On this measurement plane, the region of compressive longitudinal stress (σ_{xx}) created by rolling extends more than half-way through the thickness of the plate, to a depth of approximately 15 mm from the rolled surface (see Fig. 7). In the transverse direction (σ_{yy}) a more complex stress field arises and the modelled result indicates a small region of tensile residual stress at the rolled

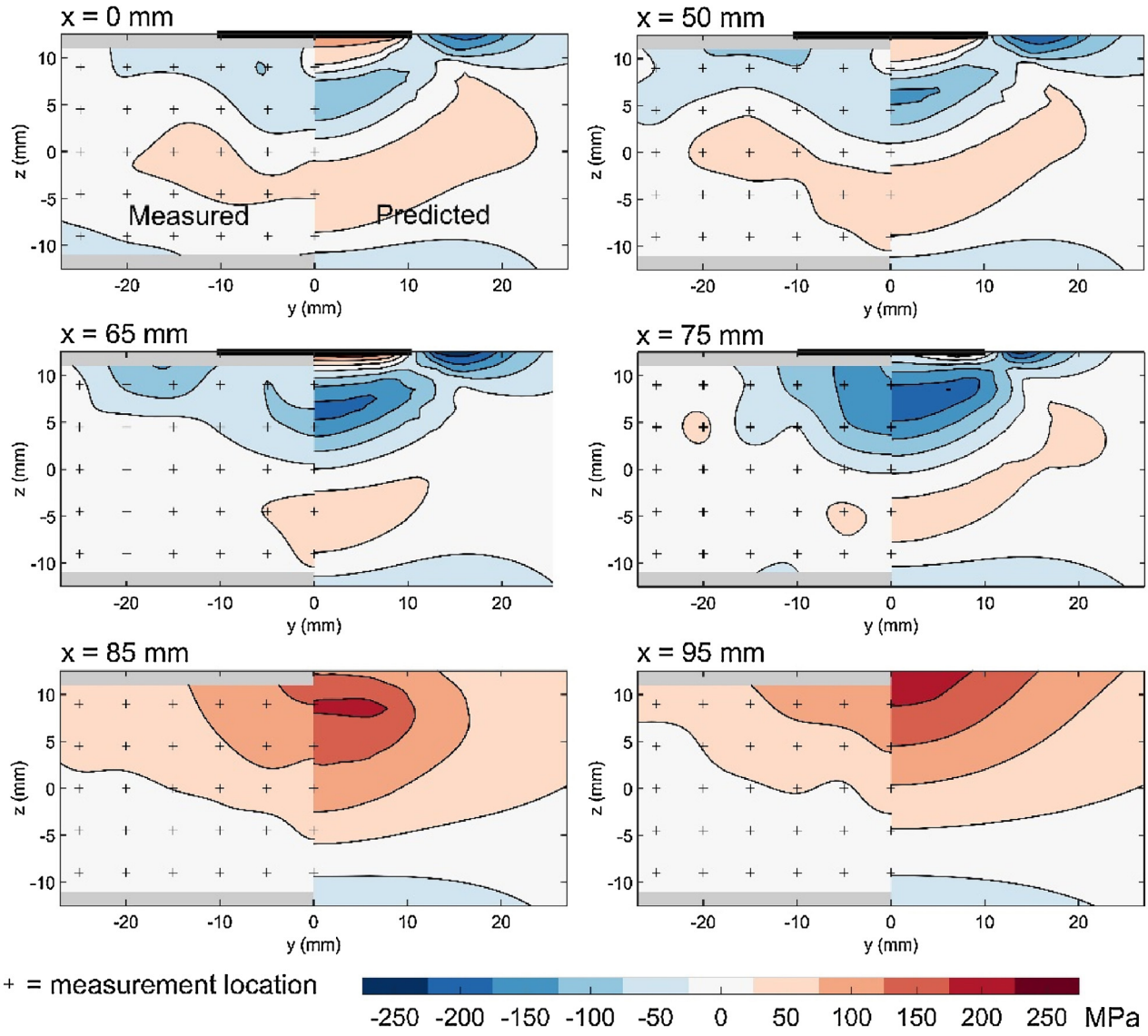


Fig. 8. Transverse residual stress (σ_{yy}) on six y-z planes within the specimen. Black crosses indicate neutron diffraction gauge volume centres and black lines at z = 12.5 indicate the roller contact zone.

surface. The FEA and ICHD results in Fig. 11 indicate large stress gradients at the upper surface of the specimen. This is also visible in the predicted stress fields in Figs. 7–9 but not in the corresponding neutron diffraction measurements, which do not extend to this surface region. Since the only significant residual stresses measured in the specimen were clearly introduced by the rolling process, the assumption that the plate was initially stress-free (used in the FE modelling) is reasonable.

The results for the planes x = 55, 65, 75, 85 and 95 mm in Figs. 7–9 illustrate the residual stress field that develops at the end of the rolled area. One important feature of the stress field here is the presence of an area of strongly tensile stress in the transverse (σ_{yy}) direction slightly beyond the end of the rolled region (see Fig. 8, x = 85 and 95 mm). Also, tensile longitudinal stress at the surface of the plate occurs beside the end of the rolled area (Fig. 7, x = 75 mm). In designs where rolling is used to create a residual stress field which is favourable to fatigue life or resistance to fracture, the presence of tensile residual stress at the surface could detrimentally promote crack growth. Therefore, it would be sensible to ensure that the end of the rolled region is remote from any areas at risk from cracking initiation. Furthermore, in the specimen examined here, concentrations of τ_{yz} shear stress occur at the edges of the rolled part of the plate along its whole length (see Fig. 9), and surface σ_{yy} stresses occur in the rolled area. The magnitude of these stress components is quite small, but they may still be significant for design purposes.

3.3. Plasticity and material flow

The distribution of plastic deformation introduced by rolling was predicted using the finite element model described in Section 2.4, and it is shown in Fig. 12. The dark blue iso-strain surface in Fig. 12a corresponds to a von Mises equivalent plastic strain of only 10 $\mu\varepsilon$, so it approximates the spatial extent of plastic straining which occurs in the specimen during rolling. The region inside this contour, in which plastic straining occurs, extends through most of the thickness of the plate directly under the roller's path and even reaches the lower surface of the plate towards the end of the rolled region. However, as shown in Fig. 12b, the region where plastic strains are greater than 10^{-2} (yellow and red areas) is much smaller and extends less than half-way through the specimen's thickness. A map of residual material displacement at the end of the rolling

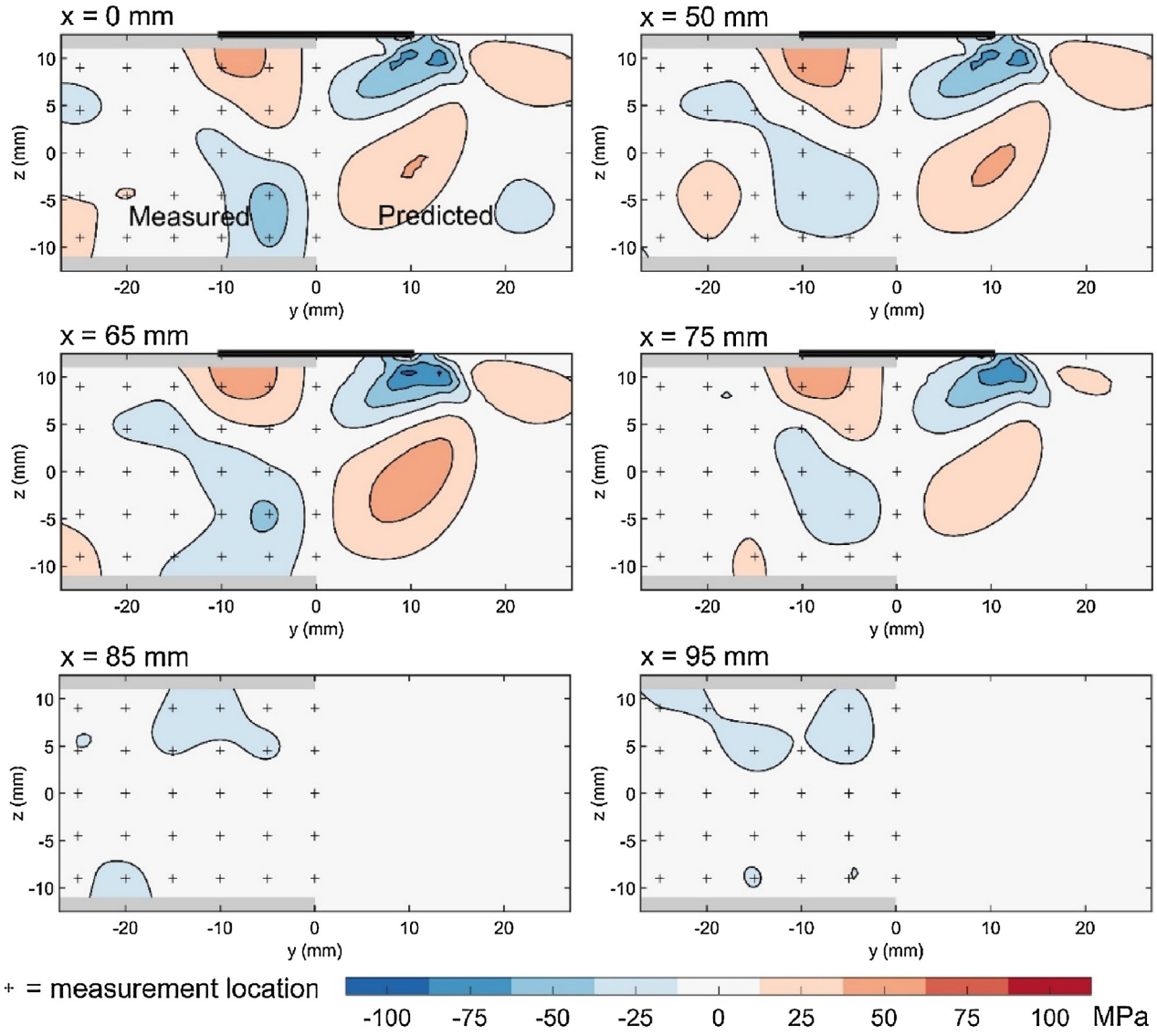


Fig. 9. Residual y-z shear stress (τ_{yz}) on six y-z planes within the specimen. τ_{yz} is anti-symmetric about the x-y plane. Black crosses indicate neutron diffraction gauge volume centres and black lines at z = 12.5 indicate the roller contact zone. Note different colour scale to Figs. 7 and 8.

process is shown in Fig. 13. The roller has pushed material directly in its path down and forward, which causes some uplift of material at the sides of the rolled region as material is pushed aside.

The distributions of residual stress (Figs. 7–9) and plasticity (Fig. 12) determined in this study vary significantly through the thickness of the plate. This contrasts with results from a previous study of much thinner (6 mm) steel welds by Coules et al. [14] in which the residual stress field varied little through the material's thickness. Together, these results support the idea that there is an upper limit to the thickness of material to which rolling can successfully relieve residual stress.

Profile measurements of the indentation caused by rolling were made using a Taylor Hobson Form TalySurf 50 contact profilometer. The surface profile of the rolled region is shown in Fig. 14. The model is completely symmetric, but the real rolling process produces an indent which is asymmetric about the centreline of the rolled region. This probably results from misalignment or flexibility in the system used for driving the roller vertically. This effect would be small in deep rolling processes where the rolling tool is spherical (or at least convex) but is noticeable with the flat roller used here. The measured residual stress data does not show significant asymmetry (see Fig. 10) so this effect must be localised to the specimen's surface. The model also over-predicts the depth of the surface indentation and the height of the ridges which form to the sides of the rolled region. This may be due to inaccuracies in modelling the contact condition which occurs between the roller and specimen, or in the plasticity model. Again, this effect is probably localised to the specimen's surface because the agreement between the modelled and measured residual stress data is good.

3.4. Use of rolling for residual stress improvement

Residual stresses in welded joints can cause fatigue life impairment and component distortion. Although several stress-relief methods have been developed, none of these are universally applicable [4]. Recently, localised rolling has been shown to create compressive residual stresses in weld seams in relatively thin materials [12–14]. A major barrier to the application of rolling to thicker welds is the uncertainty regarding the depth to which it can produce significant plastic deformation and hence modify the residual stress state. In Figs. 7–9, it can be seen that in this specimen localised rolling introduced compressive stresses to a depth

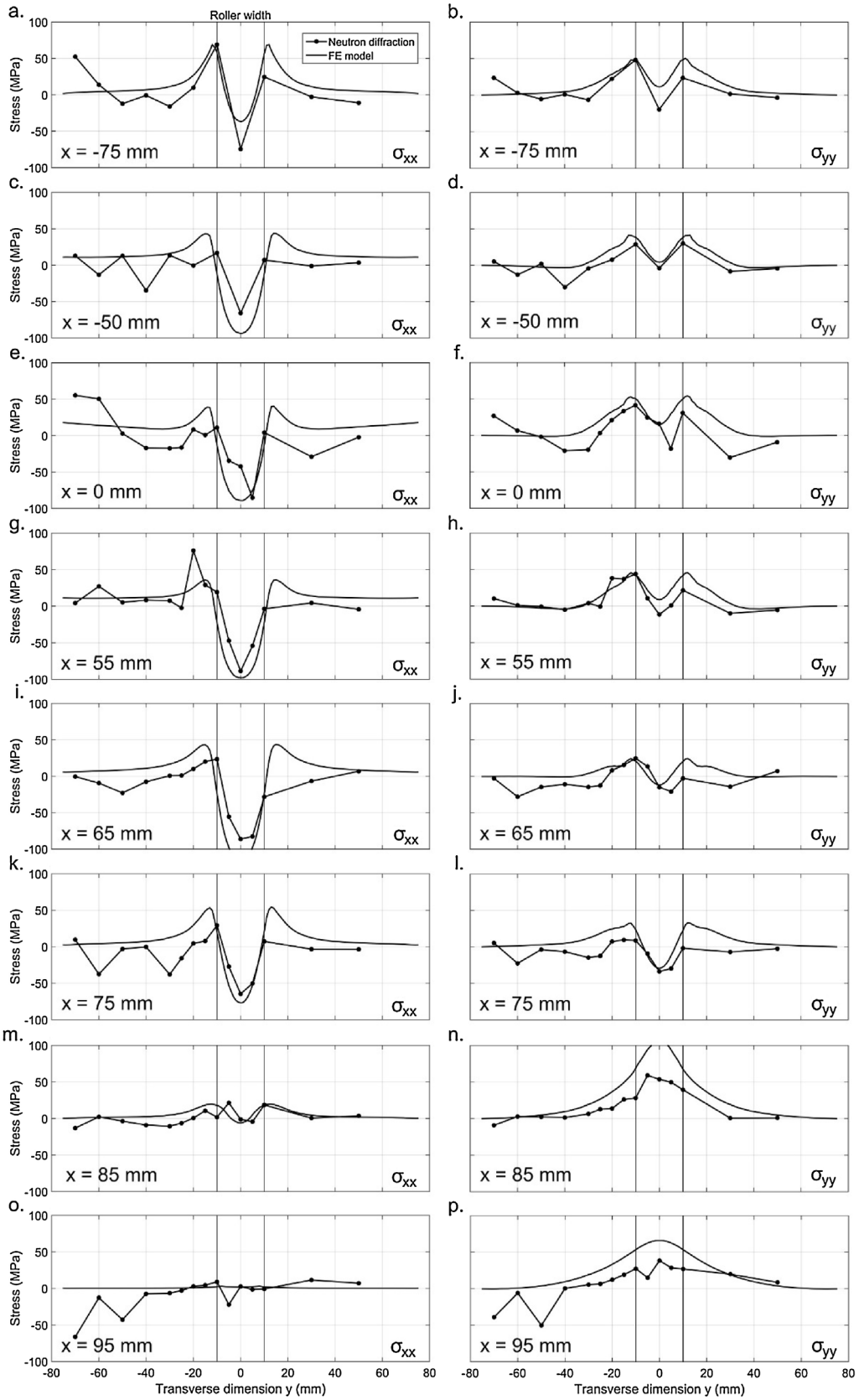


Fig. 10. Line plots longitudinal (σ_{xx}) and transverse (σ_{yy}) stress at the mid-thickness of the specimen (z = 0 mm) at eight distances along the rolled region (see in Fig. 1c). The uncertainty in the experimental measurement is approximately ±20 MPa.

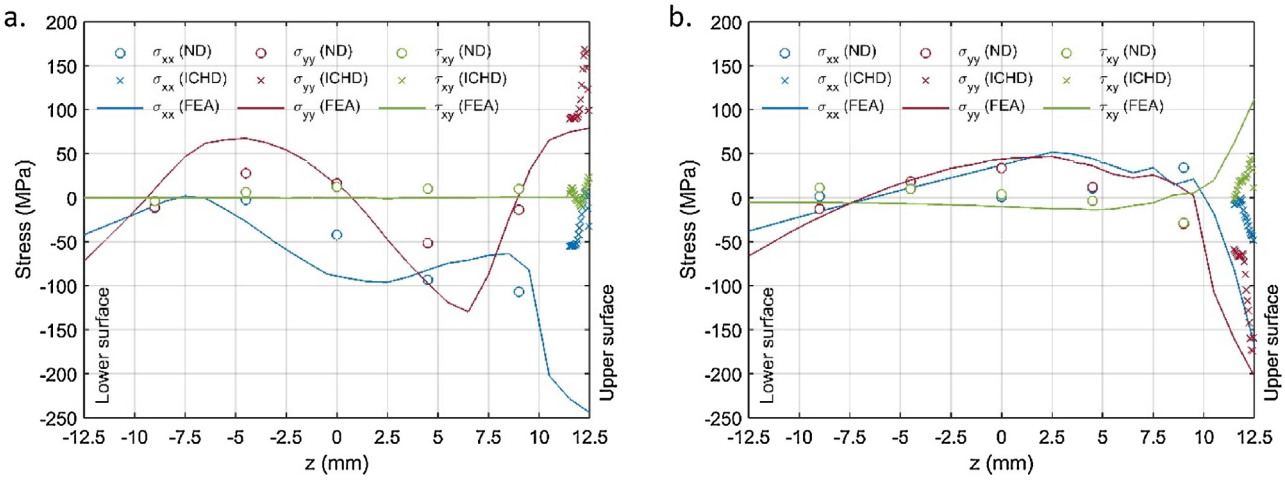


Fig. 11. Through-thickness comparison of residual stress data from Neutron Diffraction (ND), Incremental Centre Hole drilling (ICHD), and Finite Element Analysis (FEA) beneath the ICHD measurement locations shown in Fig. 1c a.) ICHD 1, b.) ICHD 2.

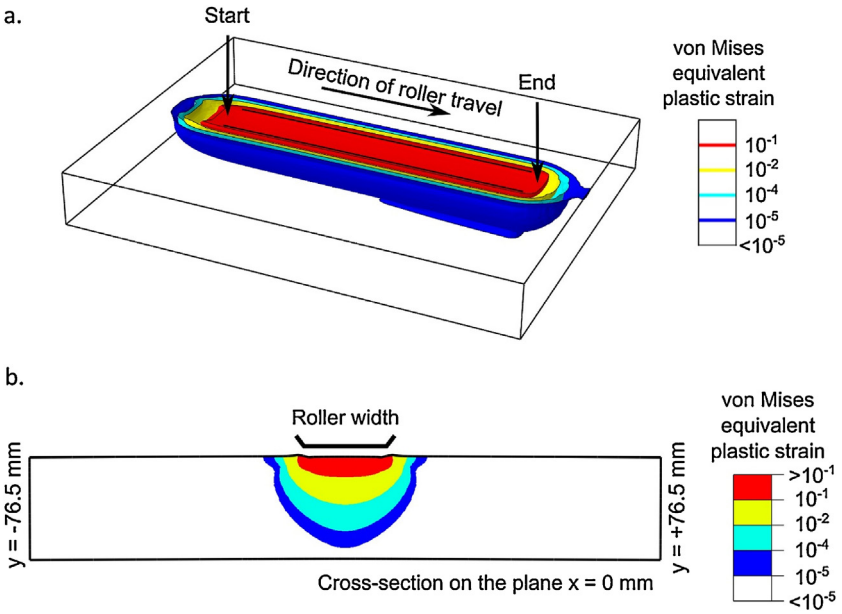


Fig. 12. Plastic strain distribution in the rolled plate after rolling predicted by finite element modelling of the rolling process. a.) Surfaces of constant plastic strain, .b) cross-section half-way along the length of the specimen (x = 0 mm). Note the logarithmic scale.

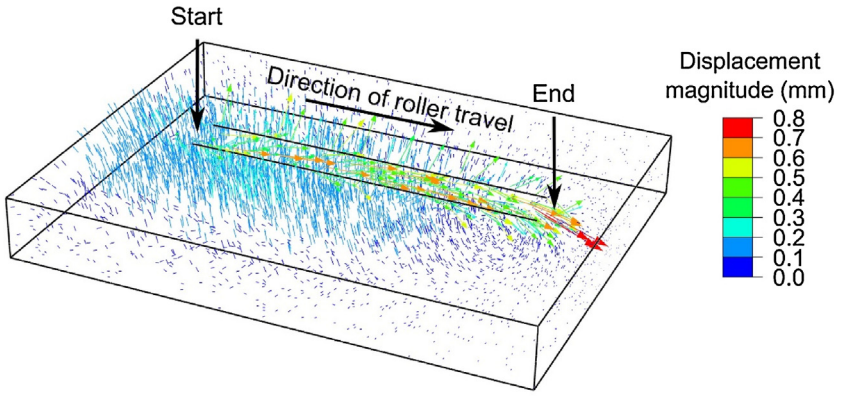


Fig. 13. Vector map of material displacement caused rolling, as calculated using the FE model. Material directly under the roller is pushed down and forward. Meanwhile there is some uplift of material the sides of the rolled region.

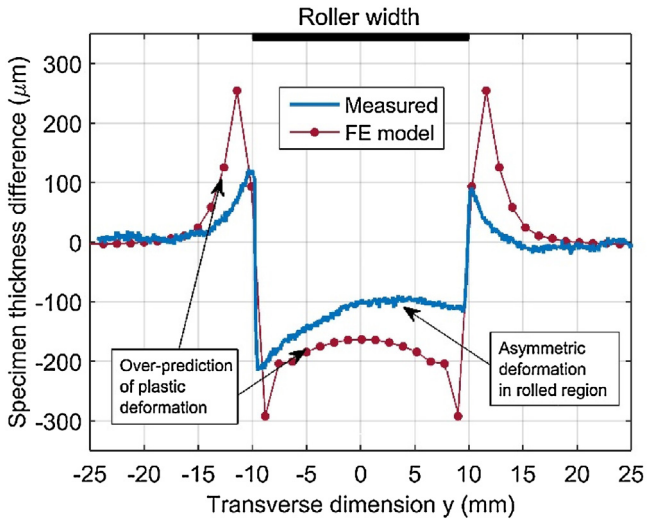


Fig. 14. The difference in specimen thickness produced by rolling, as predicted using FEA and measured using a contact profilometer.

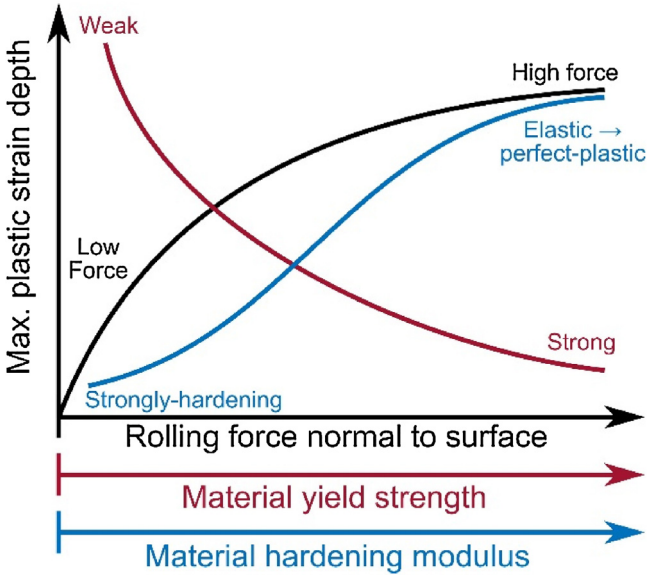


Fig. 15. Depth of effect of rolling as a function of material parameters and rolling force (schematic).

of at least 12.5 mm, i.e. more than half-way through the thickness of the material. The region in which plastic deformation occurs extends through the whole 25 mm thickness of the specimen in places (see Fig. 12). Although the material in this case is a relatively low-strength aluminium alloy, this result indicates that with sufficient material ductility rolling could be used successfully for residual stress relief of thick-section welds. The effect of the material's plastic properties and the rolling load on the depth of effect of the rolling process is shown schematically in Fig. 15. The process will produce the greatest depth of effect in low yield strength but strongly work-hardening materials, when an adequately large rolling force is applied.

The specimen used in this study was a simple stress-free plate rather than a weld. However this provides a more challenging test of the rolling process: during rolling, the significant tensile residual stresses typically present in welded joints act to cause yielding to a greater extent than in an un-welded specimen. This, in addition to the Bauschinger effect, makes it is significantly more difficult to create large compressive residual stresses using plastic deformation than to cause relaxation of pre-existing tensile residual stresses using the same process. However, it is important to note that in a real weld the yield strength of the weld material may vary significantly from that of the parent material. This strength mismatch may cause the pattern of plasticity introduced by rolling to be significantly different from that measured here for a homogenous material.

The presence of additional residual shear stresses in rolled welds has been observed in one previous experimental study [42]. In that case, as in this experiment (see Fig. 9), the magnitude of these shear stresses was small relative to the compressive stresses induced in the longitudinal and transverse directions of rolling. As a result, shear stress at the edge of rolled regions are unlikely to pose a risk to structural integrity. However, for smaller-scale deep rolling processes which are applied to an area of material using multiple parallel rolling passes, it would be advisable to overlap each pass over the previous one in order to mitigate both this shear stress effect and any tensile stress at the rolled surface.

The areas of tensile residual stress in the σ_{yy} direction that arise at the end of the rolled area in this study are important, since they could potentially promote the growth of cracks emanating from the end of the rolled region. The end effect observed in this study is consistent with the results of Lim et al. for deep rolling with multiple rolling tracks [48]. Outwards movement of material underneath the roller causes this, stretching the material beyond the rolling termination in the transverse direction. Therefore it is advisable to ensure that the termination of any rolled region occurs away from at-risk areas of a structure.

A large amount of plastic deformation may occur during rolling. In this specimen, the von Mises equivalent plastic strain directly beneath the roller was greater than 10% in a shallow region (see Fig. 12). However, the aluminium alloy used in this study exhibits rather weak strain-hardening (see Fig. 2); it is likely that in more strongly strain-hardening materials an equivalent through-depth effect of residual stress reduction could be achieved with less surface plasticity. Nevertheless, the rolling process will clearly only work well in materials which deform significantly prior to fracture. For the rolling of welds, it has been proposed that a material ductility limit must exist below which rolling cannot be successfully applied, but this limit has not yet been established [24]. The results presented here do not help to establish a ductility limit, since the specimen material was rather ductile and no problems with cracking or surface flaking were observed. However, in any material the exhaustion of ductility due to rolling-induced plasticity may affect the subsequent integrity of the rolled part.

4. Conclusions

The distribution of residual stress in an aluminium alloy plate treated using a localised rolling process has been mapped using neutron diffraction and finite element analysis. Rolling produces a region of strongly compressive residual stress underneath the roller's path. The extent of this compressive part of the residual stress field and the accompanying plastic deformation indicate that rolling could be used improve the residual stresses present in thick-section welds. Certainly, it would be feasible to treat welds up to 25 mm thick, which was the sample thickness used in this study. Although the stress field produced directly under the roller's path is generally favourable, some regions of tensile residual stress do arise as a result of rolling – particularly at the end of the rolled region. Therefore, in this weld-rolling process as well as in any analogous

deep rolling or burnishing process, the termination of the rolled area should be remote from any at-risk areas of the structure.

Acknowledgements

The authors would like to thank Dr L. D. Cozzolino and Dr K. Abburi Venkata for helpful discussions on the rolling model, and Mr A. C. Addison for assistance in producing the specimens. This work was supported by a Rolls-Royce/EDF Energy/Royal Academy of Engineering chair awarded to DJS, and an EPSRC post-doctoral fellowship (EP/M019446/1) awarded to HEC. Access to the ISIS pulsed neutron facility for the residual stress measurements was provided by the Science and Technology Facilities Council under experimental allocation no. RB1410017.

References

[1] Withers PJ. Residual stress and its role in failure. Rep Prog Phys 2007;70(12):2211–64.
[2] Budden PJ, Sharples JK. Treatment of secondary stresses. In: Ainsworth RA, Schwalbe K-H, editors. Comprehensive Structural, 7, 1st ed. Elsevier-Pergamon; 2003. p. 245–88.
[3] Withers PJ, Turski M, Edwards L, Bouchard PJ, Buttle DJ. Recent advances in residual stress measurement. Int J Press Vessels Pip 2008;85(3):118–27.
[4] Coules HE. Contemporary approaches to reducing weld induced residual stress. Mater Sci Technol 2013;29(1):4–18.
[5] Gu DD, Meiners W, Wissenbach K, Poprawe R. Laser additive manufacturing of metallic components: materials, processes and mechanisms. Int Mater Rev 2012;57(3):133–64.
[6] Delgado P, Cuesta II, Alegre JM, Díaz A. State of the art of deep rolling. Precis Eng 2016;45:1–10.
[7] Sartkulvanich P, Altan T, Jasso F, Rodriguez C. Finite element modeling of hard roller burnishing: an analysis on the effects of process parameters upon surface finish and residual stresses. J Manuf Sci Eng Trans ASME 2007;129(4):705–16.
[8] Wagner L. Mechanical surface treatments on titanium, aluminum and magnesium alloys. Mater Sci Eng A 1999;263(2):210–6.
[9] Beghini M, Bertini L, Monelli BD, Santus C, Bandini M. Experimental parameter sensitivity analysis of residual stresses induced by deep rolling on 7075-T6 aluminium alloy. Surf Coat Technol 2014;254:175–86.
[10] Nalla RK, Altenberger I, Noster U, Liu GY, Scholtes B, Ritchie RO. On the influence of mechanical surface treatments-deep rolling and laser shock peening-on the fatigue behavior of Ti-6Al-4V at ambient and elevated temperatures. Mater Sci Eng A 2003;2:216–30.
[11] Prevéy PS, Cammett JT. The influence of surface enhancement by low plasticity burnishing on the corrosion fatigue performance of AA7075-T6. Int J Fatigue 2004;26(9):975–82.
[12] Altenkirch J, Steuwer A, Withers PJ, Williams SW, Poad M, Wen SW. Residual stress engineering in friction stir welds by roller tensioning. Sci Technol Weld Join 2009;14(2):185–92.
[13] Coules HE, Colegrove P, Cozzolino LD, Wen SW, Ganguly S, Pirling T. Effect of high pressure rolling on weld-induced residual stresses. Sci Technol Weld Join 2012;17(5):394–401.
[14] Coules HE, Colegrove P, Cozzolino LD, Wen SW, Kelleher JF. High-pressure rolling of low-carbon steel weld seams: part 2 – roller geometry and residual stress. Sci Technol Weld Join 2013;18(1):84–90.
[15] Cozzolino LD. Finite Element Analysis of Localised Rolling to Reduce Residual Stress and Distortion. Cranfield University; 2013.
[16] Yang YP, Dong P. Buckling distortions and mitigation techniques for thin-Section structures. J Mater Eng Perform 2011;21(2):153–60.
[17] Colegrove PA, Coules HE, Fairman J, Martina F, Kashoob T, Mamash H, et al. Microstructure and residual stress improvement in wire and arc additively manufactured parts through high-pressure rolling. J Mater Process Technol 2013;213(10):1782–91.
[18] Martina F, Roy MJ, Szost BA, Terzi S, Colegrove PA, Williams SW, et al. Residual stress of as-deposited and rolled wire+arc additive manufacturing Ti–6Al–4V components. Mater Sci Technol 2016;32(14):1439–48.
[19] Donoghue J, Antonysamy AA, Martina F, Colegrove PA, Williams SW, Prangnell PB. The effectiveness of combining rolling deformation with wire-arc additive manufacture on $\hat{I}^2$-grain refinement and texture modification in Ti-6Al-4V. Mater Charact 2016;114:103–14.
[20] Martina F, Colegrove PA, Williams SW, Meyer J. Microstructure of interpass rolled Wire + Arc additive manufacturing Ti-6Al-4V components. Metall Mater Trans A: Phys Metall Mater Sci 2015;46(12):6103–18.
[21] Gu J, Ding J, Williams SW, Gu H, Ma P, Zhai Y. The effect of inter-layer cold working and post-deposition heat treatment on porosity in additively manufactured aluminum alloys. J Mater Process Technol 2016;230:26–34.
[22] Merwin JE, Johnson KL. An analysis of plastic deformation in rolling contact. Proc Inst Mech Eng 1963;177(1):676–90.
[23] Schajer GS, Ruud CO. Overview of residual stresses and their measurement. In: Schajer GS, editor. Practical Residual Stress Measurement Methods. 1st ed. Wiley; 2013. p. 1–27.
[24] Coules HE. Characterising the effects of high-pressure rolling on residual stress in structural steel welds. Cranfield University; 2012.
[25] BSi. 6892-1:2009 Metallic materials – tensile testing – Part 1: Method of test at ambient temperature. BSi; 2009.
[26] Chaboche JL. Constitutive equations for cyclic plasticity and cyclic viscoplasticity. Int J Plast 1989;5(3):247–302.
[27] Chaboche JL. Time-independent constitutive theories for cyclic plasticity. Int J Plast 1986;2(2):149–88.
[28] Abaqus/Standard v6.12. Providence. RI, USA: Dassault Systemes Simulia Corp.; 2012.
[29] Hutchings IM. Tribology: Friction and Wear of Engineering Materials. CRC Press; 1992.
[30] Avallone EA, Baumeister T, editors. Marks' Standard Handbook for Mechanical Engineers. 10th ed. McGraw-Hill; 1996.
[31] Holden TM. Neutron diffraction. In: Schajer GS, editor. Practical Residual Stress Measurement Methods. 1st ed. 2013: Wiley; 2017.
[32] Hutchings MT, Withers PJ, Holden TM, Lorentzen T. Introduction to the characterization of residual stress by neutron diffraction. Taylor and Francis; 2005.
[33] Krawitz AD. Neutron strain measurement. Mater Sci Technol 2011;27(3):589–603.
[34] Santisteban JR, Daymond MR, James JA, Edwards L. ENGIN-X: a third-generation neutron strain scanner. J Appl Crystallogr 2006;39(6):812–25.
[35] Larson AC, Von Dreele RB. General Structure Analysis System (GSAS). Los Alamos National Laboatory LAUR; 2004. p. 86–748.
[36] Winholtz RA. Characterization of macrostress. In: Fitzpatrick ME, Lodini A, editors. Analysis of residual stress by diffraction using neutron and synchrotron radiation. Taylor and Francis; 2003. p. 60–77.
[37] Priesmeyer HG, Schroder J. Strain tensor determination using neutron diffraction. In: Eckersey JS, Champaigne J, editors. Shot peening – theory and application. IITT-International; 1991. p. 95–100.
[38] Robinson JS, Hughes DJ, Truman CE. Confirmation of principal residual stress directions in rectilinear components by neutron diffraction. Strain 2011;47(Suppl. 2):36–42.
[39] Daymond MR, Bourke MAM, Von Dreele RB, Clausen B, Lorentzen T. Use of Rietveld refinement for elastic macrostrain determination and for evaluation of plastic strain history from diffraction spectra. J Appl Phys 1997;82(4):1554–62.
[40] Withers PJ, Preuss M, Steuwer A, Pang JWL. Methods for obtaining the strain-free lattice parameter when using diffraction to determine residual stress. J Appl Crystallogr 2007;40(5):891–904.
[41] James JA, Edwards L. Application of robot kinematics methods to the simulation and control of neutron beam line positioning systems. Nuclear Instrum Methods Phys Res Section A: Accelerators Spectrometers, Detectors Associated Equip 2007;571(3):709–18.
[42] Coules HE, Cozzolino LD, Colegrove P, Ganguly S, Wen SW, Pirling T. Neutron diffraction analysis of complete residual stress tensors in conventional and rolled gas metal arc welds. Exp Mech 2013;53(2):195–204.
[43] Wimpory RC, Ohms C, Hofmann M, Schneider R, Youtsos AG. Statistical analysis of residual stress determinations using neutron diffraction. Int J Press Vessels Pip 2009;86(1):48–62.
[44] Wimpory RC, Ohms C, Hofmann M, Schneider R, Youtsos AG. Corrigendum to štatistical analysis of residual stress determinations using neutron diffraction. Int J Press Vessels Pip 2009;86(10):721.
[45] ASTM. E837-13a Standard test method for determining residual stresses by the hole-drilling strain gauge method. ASTM International; 2013.
[46] Andersen LF. Residual Stresses and deformations in steel structures. Department of Naval Architecture and Offshore Engineering, Technical University of Denmark; 2000. p. p123.
[47] Smith MC, Smith AC, Wimpory R, Ohms C. A review of the NeT Task Group 1 residual stress measurement and analysis round robin on a single weld bead-on-plate specimen. Int J Press Vessels Pip 2014;121(1):93–140.
[48] Lim A, Castagne S, Wong CC. Effect of deep cold rolling on residual stress distributions between the treated and untreated regions on Ti-6Al-4 V alloy. J Manuf Sci Eng Trans ASME 2016;138(11).



https://dspace.org/

Three-dimensional mapping of the residual stress field in a locally rolled aluminium alloy specimen

Coules, Harry E.; Horne, G. C. M.; Kabra, S.; Colegrove, Paul A.; Smith, D. J.

2017-03-08
Elsevier
http://dx.doi.org/10.1016/j.jmapro.2017.02.010
Coules HE, Horne GCM, Kabra S, et al., (2017) Three-dimensional mapping of the residual stress field in a locally rolled aluminium alloy specimen. Journal of Manufacturing Processes, Volume 26, April 2017, pp. 240-251

Downloaded from a DSpace repository. https://dspace.org/